



Carbon supported Pd-Pt-Cu nanocatalysts for formic acid electrooxidation: Synthetic screening and componental functions

Kun Jiang, Wen-Bin Cai*

Shanghai Key Laboratory of Molecular Catalysis and Innovative Materials, Collaborative Innovation Center of Chemistry for Energy Materials, Department of Chemistry, Fudan University, Shanghai 200433, China

ARTICLE INFO

Article history:

Received 16 May 2013

Received in revised form 8 July 2013

Accepted 24 August 2013

Available online 31 August 2013

Keywords:

Multicomponent electrocatalysts

Synthetic screening

Formic acid oxidation

Surface segregation

Alloying degree

ABSTRACT

Carbon supported Pd-Pt-Cu trimetallic nanocatalysts for formic acid oxidation (FAO) are comparatively synthesized via different one-pot liquid-phase chemical reduction routes. Either sodium borohydride or ethylene glycol is employed as the main reducing agent, with the stabilizer opted from disodium ethylenediamine tetraacetate (EDTA), oleylamine, sodium citrate and urea. The trimetallic nanocatalyst synthesized with ethylene glycol and sodium citrate exhibits the most homogeneous nanoparticle dispersion and the highest alloying degree. $Pd_{20}Pt_1Cu_{10}/C-Cit$ shows the best electrocatalytic performance among all the tested electrocatalysts. Componental distributions on nanoalloy particles are distinguished through *ex situ* XPS, CO stripping and *in situ* ATR-IR measurements on interested nanocatalysts. The cheaper element Cu functions mainly as the “core filler” to expose a Pd and Pt-segregated active surface, and a deliberately controlled small fraction of Pt (versus Pd) on the surface minimizes the undesired dehydration of formic acid. In addition, a weak electronic effect from Cu and Pt may promote FAO on Pd. Surface restructuring with Pt agglomeration and partial Cu dealloying arising from a repeated potential cycling pretreatment degrades the performance of the ternary nanocatalysts.

© 2013 Elsevier B.V. All rights reserved.

1. Introduction

Formic acid (FA), as a natural biomass and avirulent non-flammable liquid, has become a promising fuel for direct liquid fed fuel cells. Direct formic acid fuel cells with a higher electromotive force (1.45 V) and a smaller crossover flux through the proton-exchange membrane as compared to direct methanol fuel cells, are a promising alternative power source for portable device applications [1,2]. Pt and Pd are two primary catalytic metals for formic acid oxidation (FAO). It is widely accepted that FAO proceeds via two main pathways, i.e., the dehydrogenation pathway to form CO_2 and the dehydration pathway to form CO followed by further oxidation to CO_2 at higher potentials. On Pt surfaces, the dehydration of FA to form the CO poisoning is facile and thus significantly retards the dehydrogenation at lower potentials [3–5] while on Pd surfaces dehydrogenation [6,7] of FA to form CO_2 predominates. Owing to its lower cost and higher activity, Pd receives more attention recently as the primary catalytic metal. However, the monometallic Pd may be rapidly deactivated owing to the CO accumulation as a result of reduction of CO_2 (the dehydrogenation product) at H-adsorbed/absorbed Pd surfaces [8,9]. Therefore, developing novel Pd-based nanocatalysts supported on carbon black with improved

activity and durability is of crucial importance for their practical applications [10,11].

The reactivity of a metallic catalyst strongly depends on its chemical and electronic properties which can be manipulated through compositionally and structurally controlled synthesis. Based on Norskov's theoretical study on strain, ensemble and ligand effects [12,13], it is possible to impart reactive intermediates with appropriate adsorption energies on the primary catalytic metal through the alloyment with another metal or metalloid, to achieve an overall enhanced electrocatalysis. Along this line, notable efforts were made to design different bimetallic Pd-based nanoalloys as the anode materials [14,15]. In fact, we have initially found that Pd-Pt bimetallic alloys with very low Pt molar fractions [16,17], exhibited superior electrocatalytic activity toward FAO.

To further upgrade the mass-specific activity of noble metals, one promising strategy is to build a core–shell structure with a non-noble metal-enriched core and a noble metal-enriched shell, by which one may take the advantages of a synergistic electronic effect between alloying elements and a higher utilization of precious metals [18,19]. Given this concern, Cu as an alloying element was used in Pt and Pd-based catalysts for several electrocatalytic reactions, like Pd-Cu alloys for FAO [20–24] and oxygen reduction reactions (ORR) [25], and Pt-based Pd-Cu@Pt/C with a quasi-core@shell structure via different post-treatments for methanol oxidation [26,27] and ORR [18,28–30]. Nevertheless, these Pt-based Pt-Pd-Cu/C catalysts where a Pt overlayer encloses a Pd-Cu alloy

* Corresponding author. Tel.: +86 21 55664050.

E-mail address: wbc@fudan.edu.cn (W.-B. Cai).



core are not suitable for efficient FAO due to the ready dehydration of FA to form CO on continuous Pt sites.

Regarding FAO, $\text{Pd}_9\text{Pt}_1/\text{C}$ [16] and $\text{Pd}_x\text{Cu}_1/\text{C}$ ($x=1$ to 3) [20–22] showed an improved electrocatalytic performance compared to Pd/C . In addition, $\text{Pd}_9\text{Pt}_1/\text{C}$ is superior to $\text{Pd}_x\text{Cu}_1/\text{C}$ in activity whereas the latter is better in durability. It is thus alluring to develop new Pd-based nanocatalysts with balanced and enhanced performances toward FAO through an appropriate compositional and structural manipulation. In this regard, Pd-based ternary nanoalloys are expected to exhibit more flexibility than binary nanoalloys in tuning the compositional, structural and electronic properties of catalytic surfaces, and thus deserve more exploration [31,32]. Nevertheless, the composition/structure-controlled one-pot synthesis of an efficient trimetallic nanocatalyst is much more challenging than that of a bimetallic one. From a practical point of view, facile synthesis of readily cleanable trimetallic Pd-based nanoalloys with favorable surface structures, particle sizes and dispersions on carbon black is highly demanded in order to maximize the utilization of Pd in the nanocatalysts as well as to achieve a higher performance.

In this work, highly dispersed ternary $\text{Pd-Pt-Cu}/\text{C}$ nanocatalysts with different alloying degrees have been obtained by screening several one-pot syntheses. X-ray diffraction, transmission electron microscopy, ICP-AES, and voltammetry and chronoamperometry are applied to examine alloying phases, morphologies, compositions, and electrocatalytic performances of the as-prepared nanocatalysts, respectively. CO stripping voltammetry, ex situ XPS, in situ ATR-IR spectroscopy and dealloying pretreatment are used to characterize surface structural and electronic effects of alloying elements Pt and Cu on the electrocatalysis of FAO on Pd-enriched surfaces of trimetallic nanoalloys.

2. Experimental

2.1. Catalyst synthesis

Synthesis of $\text{Pd-Pt-Cu}/\text{C}$ by NaBH_4 impregnation with either disodium ethylenediamine tetraacetate (EDTA) as the stabilizer in aqueous solution [16] or oleylamine (OAm) as the stabilizer in anhydrous ethanol [33] was carried out according to the previous reports with modifications. Synthesis of $\text{Pd-Pt-Cu}/\text{C}$ by polyol reduction with either sodium citrate [26] or urea [34] as the stabilizer was carried out in ethylene glycol (EG) at elevated temperatures. The as-prepared samples were noted as $\text{PdPtCu}/\text{C-EDTA}$, $\text{PdPtCu}/\text{C-OAm}$, $\text{PdPtCu}/\text{C-Cit}$, $\text{PdPtCu}/\text{C-Urea}$ respectively. The noble metal loadings for all catalysts with varying Pd/Pt atomic ratios were designed to possess the same molar quantity as that involved in 20 wt.% Pd/C. For example, in the case of $\text{Pd}_8\text{Pt}_1\text{Cu}_9/\text{C}$, we designed a noble metal loading of 17.5 wt.% Pd and 4 wt.% Pt on carbon black. Based on that, the amounts of precursors were adjusted accordingly. Detailed synthetic procedures can be found in the Supplementary Data.

The commercial catalyst of carbon-supported 40 wt.% Pd (BASF Fuel Cell Inc.), noted as Pd/C , was used as the reference sample for the electrochemical tests. Prior to its use, the Pd/C catalyst was subjected to a thermal treatment at 120 °C under a constant N_2 flow for 2 h in a tube furnace for reactivation.

2.2. Material characterizations

The chemical compositions of Pd-based nanocatalysts were analyzed by means of both energy dispersive X-ray spectrum (EDX) and inductively coupled plasma-atomic emission spectroscopy (ICP-AES) on a Thermo Elemental IRIS Intrepid. The crystalline structures were examined by X-ray diffraction (XRD) on a D8 Advance and

Davinci Design X-ray diffractometer with the $\text{Cu K}\alpha$ radiation from 30° to 90°, and the particle sizes and dispersions were characterized by (high resolution) transmission electron microscopy (HR-TEM) on a JEOL JEM-2100F microscope. The surface information of desired nanocatalysts was analyzed by X-ray photoelectron spectroscopy (XPS), carried out in a UHV system using a monochromatized $\text{Al K}\alpha$ radiation (1486.6 eV) and a Sphera II hemispherical electron energy analyzer (Omicron). The binding energies were calibrated by referencing the C 1s peak at 284.6 eV.

2.3. Electrochemical measurements

The electrochemical measurements were performed with a CHI 660B electrochemistry workstation. The electrolyte was 0.5 mol L^{-1} H_2SO_4 with or without 0.5 mol L^{-1} formic acid. All electrolytes were deaerated with high-purity Ar prior to and throughout the measurements.

The working electrode was a thin layer of Nafion-impregnated catalyst cast on a glassy carbon rotating disk electrode (GC-RDE, 3 mm diameter, 0.07 cm^2) prepared as follows: a catalyst slurry was first prepared by mixing 1 ml of $\text{C}_2\text{H}_5\text{OH}$, 2 mg of catalyst and 120 μL of Nafion (5 wt.%, Aldrich), sonicated for 1 h to obtain the catalyst ink. 5.6 μL of this ink was transferred onto a freshly polished GC-RDE via a pipette, with a constant Pd loading of 28 $\mu\text{g cm}^{-2}$ (or the same mole of Pd + Pt). A Pt gauze was used as the counter electrode, and a $\text{Hg}/\text{Hg}_2\text{SO}_4$ electrode as the reference electrode. All potentials reported are with respect to a reversible hydrogen electrode (RHE) in this work. The GC-RDE was controlled at 1000 rpm by a speed regulator provided by Tacussel Electronics (France). All electrochemical experiments were carried out at 30 ± 1 °C.

For CO stripping voltammetry, a working electrode began with bubbling CO (>99.9% purity) in solution for 20 min at 0.1 V. Then, the dissolved CO was removed from the electrolyte by bubbling Ar for 40 min while maintaining the electrode potential at 0.1 V. Finally, we recorded the CO stripping voltammograms by scanning the potential from 0.05 to 1.22 V at 10 mV s^{-1} .

The dealloying process was achieved with given cycles of voltammetric scans between 0.4 V and 0.65 V, locating at the Cu redox region while ahead of Pd oxidation. Thereafter, a full scan from 0.05 V to 1.05 V at a scan rate of 50 mV s^{-1} was applied to monitor the corresponding electrochemical response.

2.4. In situ ATR-IR measurement

The ATR-IR measurement was run on a Pd/C or $\text{Pd}_{20}\text{Pt}_1\text{Cu}_{10}/\text{C}$ catalyst layer-covered Au film on a hemicylindrical Si prism using a Varian 3100 FT-IR Excalibur spectrometer equipped with an MCT detector at a spectral resolution of 8 cm^{-1} with an unpolarized IR radiation at an incidence angle of ca. 65°. A Pt gauze was used as the counter electrode and a $\text{Hg}/\text{Hg}_2\text{SO}_4$ electrode as the reference electrode. A CHI 660B electrochemistry workstation was employed for potential control. All the spectra were shown in the absorbance unit as $-\log(I/I_0)$, where I and I_0 represent the intensities of the reflected radiation of the sample and reference spectra, respectively. ATR-IR experimental details regarding the electroless deposition of the Au film and the spectral cell setup can be found elsewhere [9,35]. The catalyst ink preparation and its transfer onto the Au film has been described in Section 2.3, with the total noble metal molar quantity loaded on the Au film equivalent to that of 45 $\mu\text{g cm}^{-2}$ of Pd.

3. Results and discussion

3.1. Synthetic methods and resulting catalysts

In the search of an appropriate synthesis to achieve highly dispersed Pd-Pt-Cu trimetallic nanoparticles (NPs) on carbon black

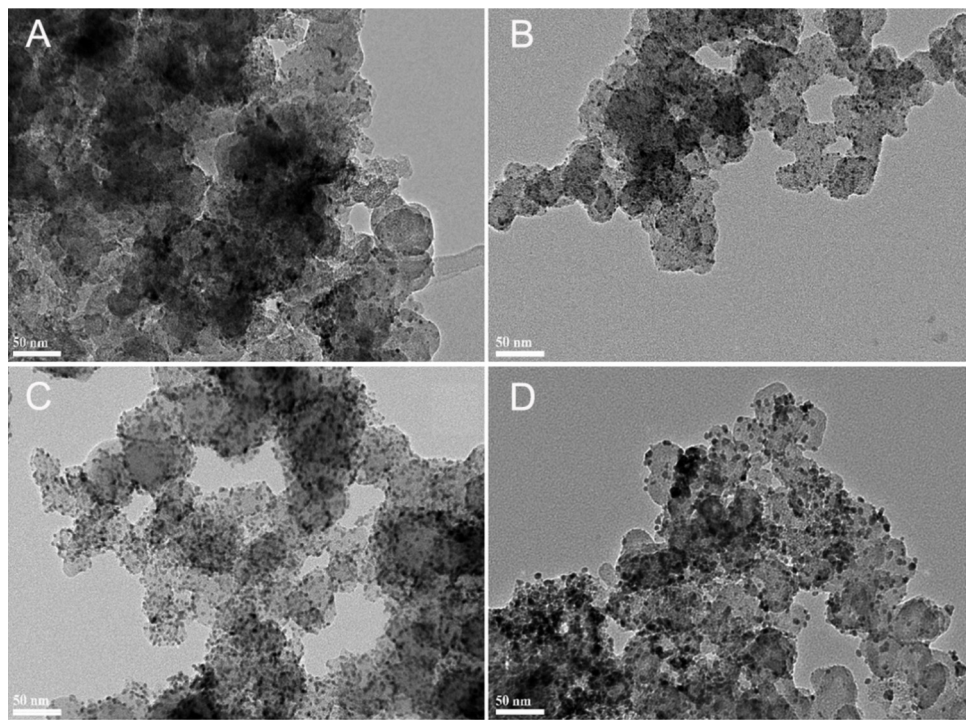


Fig. 1. TEM images of Pd-Pt-Cu/C prepared from different methods: (A) PdPtCu/C-EDTA, (B) PdPtCu/C-OAm, (C) PdPtCu/C-Cit, (D) PdPtCu/C-Urea. Scale bar for all images is 50 nm.

with controlled size distribution, we screened the NaBH_4 impregnation method with EDTA or oleylamine as the stabilizer and the EG reduction method with sodium citrate or urea as the stabilizer, for a given molar ratio 8:1:9 for Pd, Pt and Cu in precursor solutions.

Fig. 1 shows the typical TEM images of the as-prepared PdPtCu/C-EDTA (A), PdPtCu/C-OAm (B), PdPtCu/C-Cit (C) and PdPtCu/C-Urea (D). Nanoparticle agglomerations can be seen for PdPtCu/C-EDTA and PdPtCu/C-Urea samples, although the corresponding methods were effective for preparing well-dispersed Pt-based NPs on carbon black [16,34]. In contrast, a better control of nanoparticle size and dispersion was achieved for PdPtCu/C-OAm and PdPtCu/C-Cit samples, with the average particle size of 3.0 nm for the former and that of 4.1 nm for the latter. In other words, non-aqueous synthetic routes yield better nanoparticle dispersion than aqueous ones, which may be ascribed to the hydrophobic property of carbon supports. Detailed TEM characterization with different scale bars of these two samples synthesized from non-aqueous media are shown in Fig. 2.

In the synthesis of PdPtCu/C-OAm, the strong capping agent OAm and the strong reducing agent NaBH_4 facilitates a fine size control over deposited metallic NPs (Fig. 2A–C). Unlike a typical colloidal method involving organic solvents [36], the synthetic method in this work involves a least amount of OAm as the stabilizer. As a result, the adsorbed OAm can be readily removed from nanoparticle surfaces by successive rinses with copious amount of Milli-Q water and ethanol, leading to a reasonable electrochemical response of the PdPtCu/C-OAm catalyst (vide infra). In the polyol synthesis of PdPtCu/C-Cit (Fig. 2B–D), sodium citrate was added to improve the monodispersity of metallic NPs on carbon supports, and can be easily removed from nanoparticle surfaces by a similar rinse process.

In all synthetic processes, the actual molar quantity of a noble metal in an as-prepared nanoalloy was approximately identical to that in a precursor solution, while that of Cu was dependent on synthetic protocol. As for the two well-dispersed catalysts, i.e., PdPtCu/C-OAm and PdPtCu/C-Cit, a given molar ratio of 8:1:9 for Pd, Pt and Cu species in the precursor solutions yield actually

the $\text{Pd}_8\text{Pt}_1\text{Cu}_9/\text{C-OAm}$ with 16.5 wt. % Pd and the $\text{Pd}_8\text{Pt}_1\text{Cu}_5/\text{C-Cit}$ with 18.1 wt.% Pd according to the ICP-AES analysis (Note: some uncertainty of the ICP-AES measurement may explain the bias of the determined Pd loading from a targeted value of 17.5 wt % as explained in Section 2.1). Moreover, with the EG-Citrate method, a precursor solution containing an equal mole quantity of Pd and Cu leads to $\text{Pd}_2\text{Cu}_1/\text{C}$ with a loading of 20.2 wt.% Pd. It is not well understood what causes the significant loss of the less-noble metal Cu while keeping the Pd and Pt compositions in the as-synthesized catalysts [27]. Increasing the temperature and the reduction time in the polyol process may overcome this problem, however, doing so may sacrifice the nanoparticle dispersion [26].

Fig. 3 shows the corresponding XRD patterns of different Pd-based nanocatalysts. The (1 1 1) diffraction peak of $\text{Pd}_2\text{Cu}_1/\text{C}$ is centered at $\sim 42^\circ$, and that of $\text{Pd}_9\text{Pt}_1/\text{C}$ at $\sim 40^\circ$. The (1 1 1) peak for the trimetallic nanoalloys is situated in between, indicating the formation of a trimetallic alloy phase. Furthermore, slower scan fine XRD patterns inserted in Fig. 3 indicates a higher alloying degree for PdPtCu/C-Cit sample, and the presence of other phases including the PdCuO_x impurity [37] in PdPtCu/C-OAm catalyst. In contrast to the room temperature used in the NaBH_4 impregnation method, the elevated temperature used in the EG reduction method facilitates the atomic diffusions, giving rise to an improved alloying degree. According to previous reports [38], a better alloying degree may somehow impart a nanocatalyst with an improved electrocatalytic performance.

3.2. Electrocatalytic performances toward FAO

Fig. 4A shows cyclic voltammograms recorded for Pd/C, Pd-Cu/C and Pd-Pt-Cu/C in 0.5 M H_2SO_4 solution. Hydrogen adsorption/desorption peaks occurred for all catalysts below 0.35 V, and the broad peak located at around 0.5–0.6 V was assigned to the redox peak of the alloyed Cu. Unlike the unsupported Pd-Cu nanocatalyst prepared by the galvanic redox replacement of initial PVP-protected Cu NPs [21], only very small anodic current peaks

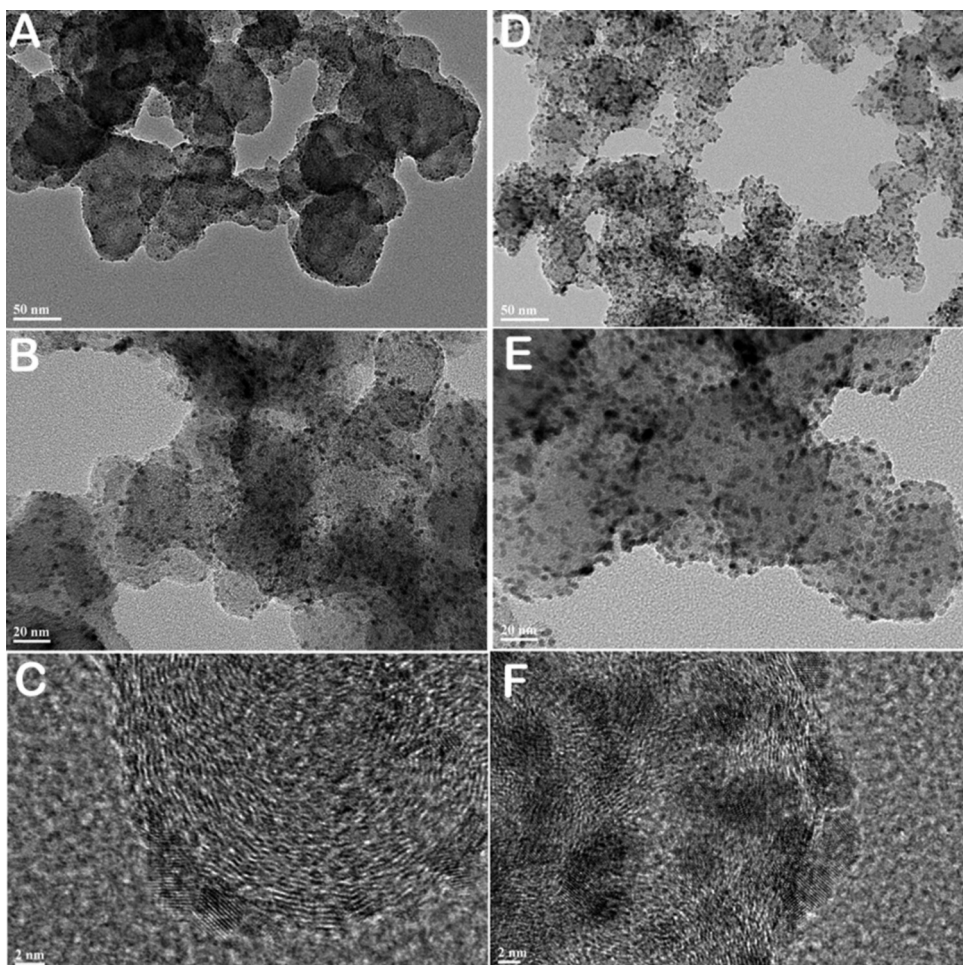


Fig. 2. (HR)TEM images of PdPtCu/C-OAm (A, B, C) and PdPtCu/C-Cit (D, E, F) catalysts at different scale bars: for (A and D) is 50 nm, for (B and E) is 20 nm, for (C and F) is 2 nm.

due to the dissolution of alloyed Cu (rather than unalloyed Cu) were observed on these three nanocatalysts, suggestive of a low Cu molar fraction on the surface and an improved alloying degree, stabilizing Cu in the nanocatalysts.

The electrocatalytic activities of these catalysts were examined in a 0.5 M H_2SO_4 + 0.5 M FA solution by cyclic voltammetry as shown in Fig. 4B where the current density was normalized to the geometric area of a GC electrode. Compared with the Pd/C, the

bimetallic and trimetallic catalysts exhibit oxidation peak currents 1.5 to 1.7 times as high (positive scan) toward FAO. In addition, the alloying with a low percentage of Pt favors a negative shift of the oxidation peak potential, in analogy to that observed for our $\text{Pd}_x\text{Pt}_{1-x}$ alloys [16,17]. Fig. 4C shows the chronoamperometric curves recorded at 0.45 V with a disk electrode rotated at 1000 rpm. PdCu/C-Cit bimetallic catalyst shows the highest FAO current density at 3000 s, i.e., 9.0 mA cm^{-2} , among all the tested samples. PdPtCu/C-OAm catalyst, however, does not show any advantage in this stability test, the current density at 3000 s is more or less like that for Pd/C (i.e., 2.2 mA cm^{-2}), despite a much higher initial activity. The more rapid electrocatalytic activity decay of PdPtCu/C-OAm may be attributed to (i) a poorer alloying degree of PdPtCu/C-OAm as already shown in XRD patterns, and (ii) the presence of contiguous Pt sites on PdPtCu/C-OAm leading to accumulated CO poisoning species [39,40] as indicated from a much smaller oxidation current in the forward scan than in the backward scan in Fig. 4B. In contrast, the PdPtCu/C-Cit yields a more durable catalytic activity, in consistent with an improved alloying degree and more isolated single Pt sites on PdPtCu/C-Cit surfaces.

On the basis of the above TEM, XRD and electrochemical characterizations, the $\text{Pd}_8\text{Pt}_1\text{Cu}_5/\text{C-Cit}$ catalyst is regarded very promising for FAO, with a narrow size distribution, a high alloying degree and a good dispersion on carbon support. Despite a strikingly negative shift of peak potential for FAO, $\text{Pd}_8\text{Pt}_1\text{Cu}_5/\text{C-Cit}$ is yet inferior to $\text{Pd}_2\text{Cu}_1/\text{C-Cit}$ regarding the long-term activity. As continuous surface Pt sites favor the dehydration of formic acid to form CO

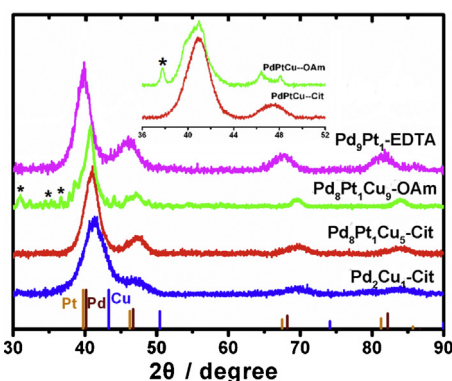


Fig. 3. XRD patterns of different Pd-based nanocatalysts. The inset picture shows a regional pattern for PdPtCu/C-OAm and PdPtCu/C-Cit samples from 20 degree of 36° to 52° at a slower scan rate, PdCuO_x oxides was indicated by *.

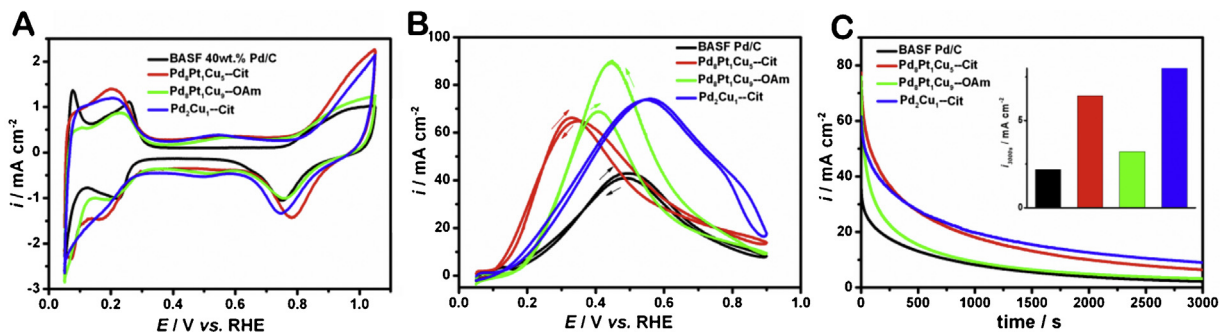


Fig. 4. (A) Cyclic voltammograms on Pd-based/C catalysts in 0.5 M H₂SO₄ at a scan rate of 50 mV s⁻¹; (B) cyclic voltammograms recorded at 50 mV s⁻¹ and (C) chronoamperometric curves recorded at 0.45 V for selected Pd-based/C catalysts coated GC-RDEs in 0.5 M H₂SO₄ + 0.5 M HCOOH solution at a rotation speed of 1000 rpm; the inset is the comparison of current density at 3000 s (i_{3000s}).

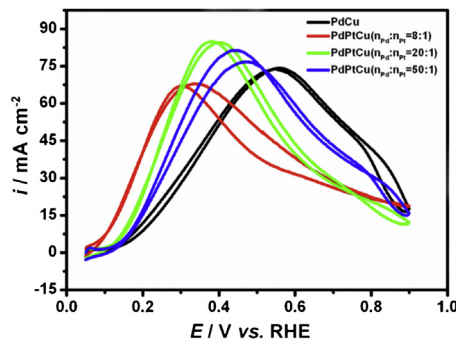


Fig. 5. Cyclic voltammograms recorded at 50 mV s⁻¹ for selected Pd-based/C-Cit catalysts in 0.5 M H₂SO₄ + 0.5 M HCOOH solution at a rotation speed of 1000 rpm.

[39], one solution to this problem is to reduce the amount of Pt in the trimetalllic alloy [31] while maintaining the same molar ratio of (Pd + Pt) to Cu in initial precursors for the EG-Citrate synthetic route. As a result, we actually obtained Pd₈Pt₁Cu₅, Pd₂₀Pt₁Cu₁₀, and Pd₅₀Pt₁Cu₂₇. Notably, all the Pd-Pt-Cu/C-Cit catalysts prepared via this route show a similar size distribution, a high dispersion of metallic NPs as well as an essentially same total molar quantity of noble metals on carbon support, regardless of varying Pt/Pd molar ratios (see Supplementary Data, Fig. S1).

Fig. 5 illustrates the cyclic voltammograms of the resulting PdPtCu/C-Cit catalysts in 0.5 M H₂SO₄ and 0.5 M HCOOH. Obviously, the oxidation peak potential shifts negatively accompanied with an increasing hysteresis of forward and backward-scan voltammograms in response to the increase of Pt content. Table 1 lists several parameters related to electrocatalytic performances of these Pd-based/C nanocatalysts. Notably, i₃₆₀₀ was adapted from the current versus time plot at a constant oxidation potential for an as-synthesized nanocatalyst, serving as an indicator for its durable activity. The relevant chronoamperometric curves are shown in the supplementary data (Fig. S2).

From Table 1, we can see that given an approximately same molar ratio of (Pd + Pt) to Cu (i.e., ca. 2:1), a trace amount of Pt enhances the electrocatalytic performance toward FAO. Notably, significantly enhanced electrocatalysis was also observed on Pd₁₉Pt₁/C [41] for hydrogen oxidation, and on Pd adatoms-decorated Pt NPs [42] and Pd₉Pt₁/C [16] for FAO, which may be ascribed to an appropriate decrease of d-band center of Pd in the presence of sufficiently isolated surface Pt sites. In this work, both Pd₂₀Pt₁Cu₁₀/C-Cit and Pd₅₀Pt₁Cu₂₇/C-Cit showed an improved long-term activity as compared to Pd₂Cu₁/C-Cit and the commercial Pd/C. Also we should point out that the best bimetallic Pd-Pt/C nanocatalyst so far synthesized (i.e., Pd₉Pt₁/C) exhibits a more rapid oxidation current decay, for example, ca. 9.0 mA cm⁻² at t = 1200 s, measured under otherwise same conditions [16]. In addition, Pd₂₀Pt₁Cu₁₀/C-Cit exhibits a more negative oxidation peak potential and a higher oxidation peak current as compared to Pd₅₀Pt₁Cu₂₇/C-Cit.

3.3. Componential distributions and functions

So far, we have screened an appropriate one-pot synthesis for Pd-based Pd-Pt-Cu/C nanocatalysts, and identified that Pd₂₀Pt₁Cu₁₀/C-Cit and Pd₅₀Pt₁Cu₂₇/C-Cit exhibited a balanced improvement in electrocatalysis of FAO in terms of activity and durability over Pd/C, Pd-Pt/C and Pd-Cu/C bimetallic nanocatalysts. Next, we will further discuss the component functions and surface segregation of noble metals by applying ex situ XPS, CO stripping and in situ ATR-IR measurements mainly on Pd₂₀Pt₁Cu₁₀/C-Cit for case study.

Ex situ XPS analysis was carried out to evaluate both the near-surface composition and core level binding energy on Pd₂₀Pt₁Cu₁₀/C-Cit. The atomic ratio of 10.3:1:2.7 for Pd, Pt and Cu (or 4:1 for (Pd + Pt)/Cu) obtained in the top layers suggests a nanostructure of "Cu-enriched core and Pd and Pt-enriched surface" (as compared to the bulk compositions of 20:1:10 for Pd:Pt:Cu). Fig. 6 shows the core level XPS spectra for Cu 2p, Pd 3d and Pt 4f regions in Pd₂₀Pt₁Cu₁₀/C-Cit. The binding energy for Pd⁰ 3d_{5/2} shifts to a higher value (ca. 335.4 eV) as compared to that on Pd/C of 334.9 eV, whereas the binding energy for Cu⁰ 2p_{3/2} shifts to a lower value (ca. 932.0 eV) as compared to standard Cu⁰, 932.4 eV, providing an proof for the partial charge transfer from Cu to Pd and a resulted lower d-band center of Pd [20,25,43]. In addition, the binding energy for Pt⁰ 4f_{7/2} is virtually unshifted (ca. 0.1 eV), suggestive of a negligible electronic effect from Pt on Pd in this trimetalllic nanoalloy.

Fig. 7A shows the base voltammograms in 0.5 M H₂SO₄ and the CO stripping voltammograms of four different catalysts. The enlarged plots in Fig. 7B show that the onset oxidation potential for CO on an alloyed catalyst shifts negatively by ca. 50 mV, compared to that on Pd/C, suggesting a weakened CO adsorption on the

Table 1
Summary of electrocatalytic performance for tested nanocatalysts.

Samples	E _{peak} /V	i _{peak} /mA cm ⁻²	i ₃₆₀₀ /mA cm ⁻²
BASF Pd/C	0.49	42.9	1.7
Pd ₂ Cu ₁ /C	0.56	74.2	7.5
Pd ₈ Pt ₁ Cu ₅ /C	0.30	67.1	5.1
Pd ₂₀ Pt ₁ Cu ₁₀ /C	0.37	84.9	8.9
Pd ₅₀ Pt ₁ Cu ₂₇ /C	0.45	81.3	9.0

The peak current (i_{peak}) and potential (E_{peak}) refers to forward scan only, recorded at 50 mV s⁻¹, the current density (i₃₆₀₀) is measured by chronoamperometry for a duration of 3600 s at 0.45 V in 0.5 M H₂SO₄ + 0.5 M HCOOH solution at a rotation speed of 1000 rpm.

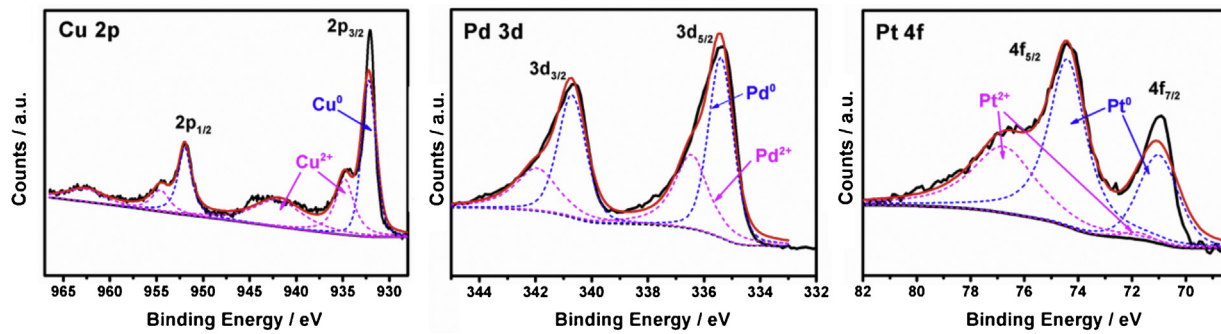


Fig. 6. Core level XPS spectra for Cu 2p, Pd 3d and Pt 4f regions of $\text{Pd}_{20}\text{Pt}_1\text{Cu}_{10}/\text{C-Cit}$ nanocatalyst.

former. This may be ascribed to the proper downshift of Pd d-band center due to its alloying with Cu and Pt and a higher oxygen affinity of a few exposed surface Cu sites [44,45] which boost the oxidative removal of CO_{ad} .

As can be seen from the current response in the hydrogen adsorption/desorption potential region as well as the cathodic peak area related to the reduction of Pd-Pt oxides at 0.75 V, the electrochemically active surface area of a Pd-Cu or Pd-Pt-Cu nanocatalyst is significantly increased as compared to that of Pd/C. Since the molar quantity of Pd for each catalyst loaded on a GC substrate is same in voltammetric measurement in Fig. 7, and the mean metallic nanoparticle size for each sample is nearly same, or ca. 4 nm as characterized from TEM [46], it may be concluded that the alloying with Cu yields a larger population of metallic NPs for electrocatalysis measurement. In this regard, the cheap Cu acts as a core-filler in the core-shell-like structure of Pd-Pt-Cu NPs. From XPS measurement, the Pd/Pt site ratio on the trimetallic nanoalloy surface is about 10:1, which means that Pt atoms are sufficiently diluted

and isolated, as it was desired for blocking the FA dehydration pathway and promoting the FA dehydrogenation pathway on Pt sites. Meanwhile, together with Cu the sparsely populated Pt sites on the surface may contribute to a slight but favorable electronic modification on surface Pd sites, i.e., an appropriate downshift of the d-band center of Pd (as deduced from the Pd core-level shift in the above XPS spectra). According to Norskov's theory, the d-band center decides the adsorption strength of surface species [13], only a moderate downshift is optimized for enhanced FAO. Since the hydrogen oxidative desorption peak position reflects qualitatively the H-adsorption strength on Pd sites (thus the d-band center of Pd) [47], the peak position observed in the order $\text{Pd/C} > \text{Pd}_2\text{Cu}_1/\text{C-Cit} > \text{Pd}_{20}\text{Pt}_1\text{Cu}_{10}/\text{C-Cit} > \text{Pd}_8\text{Pt}_1\text{Cu}_5/\text{C-Cit}$ (see Fig. S3 in the supplementary data) is in reasonable agreement with the optimized performance found for $\text{Pd}_{20}\text{Pt}_1\text{Cu}_{10}/\text{C-Cit}$.

A Pd-enriched surface with a slightly modified electronic property may be further inferred by comparing in situ ATR-IR spectra of CO adsorption on $\text{Pd}_{20}\text{Cu}_1\text{Pt}_{10}/\text{C-Cit}$ and Pd/C, since the $\nu(\text{CO})$

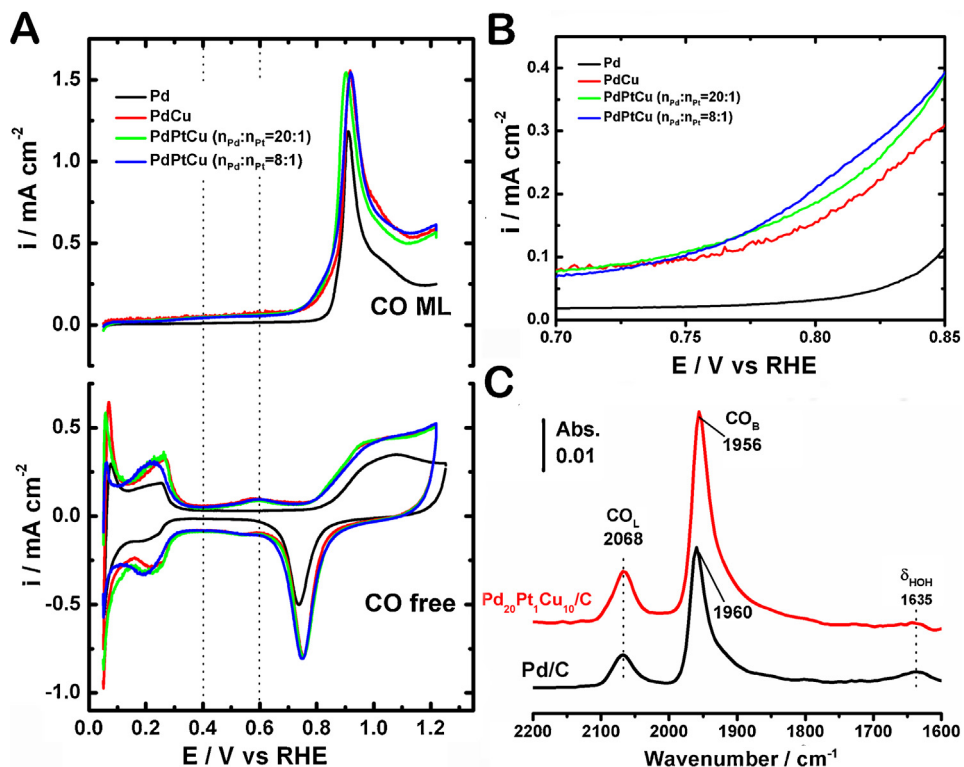


Fig. 7. (A) CO stripping voltammograms on Pd-based/C-Cit catalysts in 0.5 M H_2SO_4 at a scan rate of 10 mV s^{-1} ; (B) zoomed current vs. potential responses in the onset stripping region of CO on the four catalysts; (C) ATR-IR spectra for the adsorption of CO on Pd/C (black line) and $\text{Pd}_{20}\text{Pt}_1\text{Cu}_{10}/\text{C-Cit}$ (red line) modified Au film electrodes at 0.1 V in CO-saturated 0.5 M H_2SO_4 .

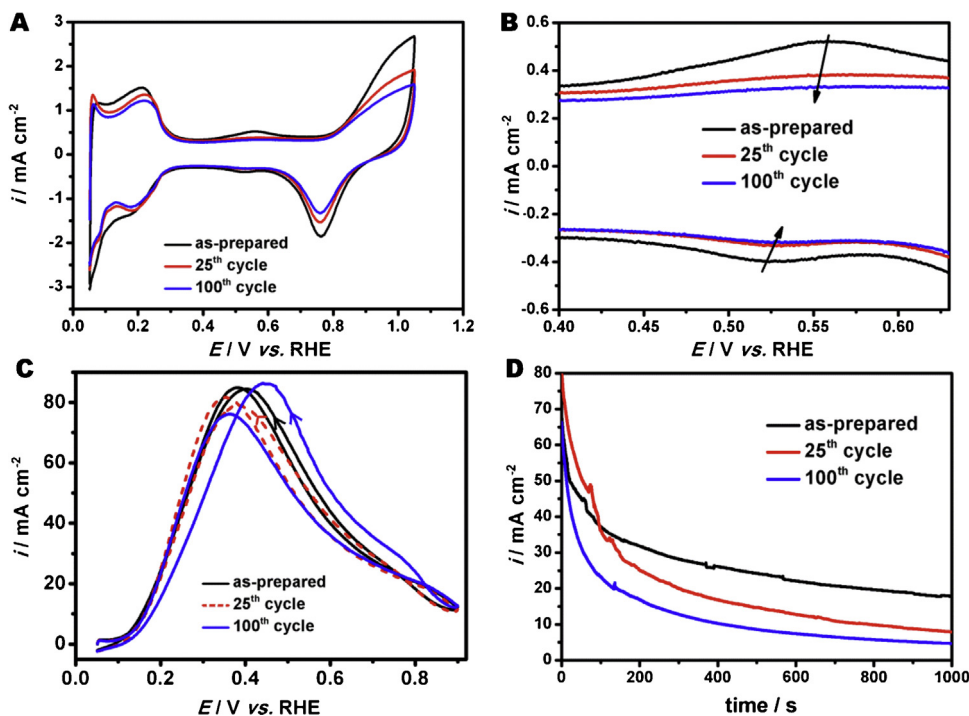


Fig. 8. (A) Evolution of the voltammetric profiles of Pd₂₀Pt₁Cu/C-Cit during dealloying process in 0.5 M H₂SO₄ at a scan rate of 50 mV s⁻¹; (B) magnified CV region from Fig. 8A; (C) cyclic voltammograms at a scan rate of 50 mV s⁻¹ and (D) chronoamperometric curves recorded at 0.45 V of Pd₂₀Pt₁Cu₁₀/C-Cit with different dealloyed extent in 0.5 M H₂SO₄ + 0.5 M HCOOH solution, at a rotation speed of 1000 rpm.

frequency is very sensitive to adsorption sites and types of metals [48]. In fact, when the elemental mapping is hard to perform on the nanoparticles with a size below 5 nm, such a combination of XPS and ATR-IR measurements may provide useful clues on surface information. Fig. 7C shows the typical ATR-IR spectra of CO on Pd/C (black line) and Pd₂₀Pt₁Cu₁₀/C-Cit (red line) in CO-saturated 0.5 M H₂SO₄ at 0.1 V, where the reference spectra were taken in Ar-saturated 0.5 M H₂SO₄ solution at 0.1 V. (For interpretation of the references to color in this figure legend, the reader is referred to the web version of the article.) The band at 2068 cm⁻¹ is attributable to linear adsorbed CO (CO_L), while the band at 1956 or 1960 cm⁻¹ to bridge-bonded CO (CO_B). It is noteworthy that the CO_{ad} band features inclusive of relative positions and intensities of CO_L and CO_B for the two measurements are very close, suggesting that surface Pt and Cu molar fractions are too low to affect the CO spectral features on Pd sites in the trimetallic nanoalloy. In addition, these spectral features match well with those reported on a Pd film electrode [8,35], demonstrating that the as-prepared nanocatalysts are in fact enclosed with Pd enriched surfaces. In contrast, a significant band around 2100 cm⁻¹ was observed and assigned to CO_L on abundant Cu sites for previously reported Pd-Cu bulk alloys [49,50]. On the other hand, the CO_B band is generally considered as a mark to characterize the electron density of surface Pd sites. Here, a red-shift of 4 cm⁻¹ of CO_B on Pd₂₀Pt₁Cu₁₀/C-Cit compared to that on Pd/C suggests a partial charge transfer from Cu to Pd and a down-shift of the d-band center of Pd, in agreement with the above discussion.

In order to demonstrate the important roles of Cu and Pt in the nanocatalyst, reiterative potential cycling is employed to leach Cu components and restructuring surface Pt distributions [51,52]. Fig. 8A and B shows the evolution of the voltamograms on Pd₂₀Pt₁Cu₁₀/C-Cit coated GC-RDE. It is clear that the electrochemically active surface area gradually decreases upon potential cycling. This may be attributed to particle ripening and surface restructuring concomitant with Cu leaching occurring on sub-5 nm NPs [53]. In Fig. 8C, a higher backward oxidation current accompanied with a hysteresis of oxidation peak potentials in the forward and backward

potential scans can be observed after 100 cycles, indicating the accumulation of CO_{ad} poisoning species at lower potentials resulted mainly from FA dehydration on agglomerated Pt sites and from reduction of CO₂ on Pd sites. The Pt agglomeration upon potential cycling was also noted on Pt-based Pt-Pd-Cu nanotubes by Cui et al. [51], which was used to promote the ORR. Herein, the oxidation current at 0.45 V decays more quickly with a more intense Cu dealloying, as shown in Fig. 8D. The unfavorable effect of the intense dealloying pretreatment further confirms the importance of appropriately structured Cu and Pt components in maintaining the high electrocatalysis performance of the trimetallic nanocatalyst. Fortunately, the Pd-based trimetallic nanocatalyst is to work in the anode of a direct formic acid fuel cell, and thus the potentials it experiences are much lower than those in the cathode. What's more, here Cu acts mainly as the core filler in a core–shell-like nanostructure, and the Cu content in our trimetallic catalyst is much lower than that found in Pd-Cu and Pd-Cu@Pt catalysts in previous reports [18,21,37]. As a result, the dealloying effect could be negligible, enabling a rather stable composition and structure. A minimal membrane contamination by Cu [37] may be expected if any in practice. Test of the as-synthesized catalyst in a real fuel cell may be pursued in the near future.

4. Conclusions

In order to achieve a balanced improvement on the activity and durability of Pd-based electrocatalysts for FAO, rational design and synthesis, structural analysis, performance evaluation and insightful understanding of multi-component nanoalloys are essential. In this work, we have comparatively screened several one-pot synthetic methods for preparing carbon-supported Pd-Pt-Cu nanocatalysts by varying reducing agents, solvents, and stabilizers. It turns out that nanocatalysts prepared with ethylene glycol as the dispersion solvent and reducing agent and sodium citrate as the stabilizer exhibits a narrow size distribution, a high alloying degree and a high dispersion on carbon support,

$\text{Pd}_{20}\text{Pt}_1\text{Cu}_{10}/\text{C-Cit}$ is the best one toward FAO among all tested nanocatalysts. CO stripping measurement in conjunction with ex situ XPS and in situ ATR-IR spectroscopies has been performed to qualitatively understand component distributions and roles. The trimetallic nanocatalyst thus obtained possesses a Pd and Pt segregated surface. Low molar fraction of Pt with its atoms sufficiently diluted at the surface minimizes the CO poisoning arising from FA dehydration and increases the electrocatalytic activity at lower oxidation potentials. Cu mainly functions as a “core filler” to expose more Pd and Pt active sites on the surface. In addition, Cu and Pt exert a modest but favorable electronic effect on Pd, which may weaken appropriately the binding strength of surface intermediates on Pd sites. All the above structural features and electronic effects lead to a significant and balanced improvement on the electrocatalysis performance of the $\text{Pd}_{20}\text{Pt}_1\text{Cu}_{10}/\text{C-Cit}$ for FAO. Surface restructuring with Pt agglomeration due to intense Cu dealloying procedure degrades the performance of the ternary nanocatalysts. The current work may lend new hints for the development of high performance multi-component nanocatalysts toward better clean energy utilization.

Acknowledgments

This work is supported by NSFC (Nos. 21073045 and 21273046), SMCST (Nos. 11JC140200 and 08DZ2270500). We acknowledge State Key Laboratory of Physical Chemistry for Solid Surfaces for providing the Open Project support via the coordinator Prof. Zhao-Xiong Xie (No. 201108), and Dr. Yan-Ping Zheng and Prof. Ming-Shu Chen from Xiamen University for the XPS measurements.

Appendix A. Supplementary data

Supplementary data associated with this article can be found, in the online version, at <http://dx.doi.org/10.1016/j.apcatb.2013.08.037>.

References

- [1] U.B. Demirci, *J. Power Sources* 169 (2007) 239–246.
- [2] S. Uhm, H.J. Lee, J. Lee, *Phys. Chem. Chem. Phys.* 11 (2009) 9326–9336.
- [3] A. Capon, R. Parsons, *J. Electroanal. Chem.* 45 (1973) 205–231.
- [4] G. Samjeske, A. Miki, S. Ye, A. Yamakata, Y. Mukouyama, H. Okamoto, M. Osawa, *J. Phys. Chem. B* 109 (2005) 23509–23516.
- [5] A. Cuesta, G. Cabello, M. Osawa, C. Gutierrez, *ACS Catal.* 2 (2012) 728–738.
- [6] M. Arenz, V. Stamenkovic, P.N. Ross, N.M. Markovic, *Surf. Sci.* 573 (2004) 57–66.
- [7] H. Miyake, T. Okada, G. Samjeske, M. Osawa, *Phys. Chem. Chem. Phys.* 10 (2008) 3662–3669.
- [8] J.Y. Wang, H.X. Zhang, K. Jiang, W.B. Cai, *J. Am. Chem. Soc.* 133 (2011) 14876–14879.
- [9] H.X. Zhang, S.H. Wang, K. Jiang, T. Andre, W.B. Cai, *J. Power Sources* 199 (2012) 165–169.
- [10] M. Ren, Y. Kang, W. He, Z. Zou, X. Xue, D.L. Akins, H. Yang, S. Feng, *Appl. Catal. B: Environ.* 104 (2011) 49–53.
- [11] L. Zhang, L. Wan, Y. Ma, Y. Chen, Y. Zhou, Y. Tang, T. Lu, *Appl. Catal. B: Environ.* 138–139 (2013) 229–235.
- [12] P. Liu, J.K. Norskov, *Phys. Chem. Chem. Phys.* 3 (2001) 3814–3818.
- [13] J.R. Kitchin, J.K. Norskov, M.A. Barteau, J.G. Chen, *Phys. Rev. Lett.* 93 (2004) 156801.
- [14] C. Bianchini, P.K. Shen, *Chem. Rev.* 109 (2009) 4183–4206.
- [15] J. Ge, W. Xing, X. Xue, C. Liu, T. Lu, J. Liao, *J. Phys. Chem. C* 111 (2007) 17305–17310.
- [16] H.X. Zhang, C. Wang, J.Y. Wang, J.J. Zhai, W.B. Cai, *J. Phys. Chem. C* 114 (2010) 6446–6451.
- [17] C. Wang, B. Peng, H.N. Xie, H.X. Zhang, F.F. Shi, W.B. Cai, *J. Phys. Chem. C* 113 (2009) 13841–13846.
- [18] M.H. Shao, K. Shoemaker, A. Peles, K. Kaneko, L. Protsailo, *J. Am. Chem. Soc.* 132 (2010) 9253–9255.
- [19] Y. Kang, L. Qi, M. Li, R.E. Diaz, D. Su, R.R. Adzic, E. Stach, J. Li, C.B. Murray, *ACS Nano* 6 (2012) 2818–2825.
- [20] L. Lu, L.P. Shen, Y. Shi, T.T. Chen, G.Q. Jiang, C.W. Ge, Y.W. Tang, Y. Chen, T.H. Lu, *Electrochim. Acta* 85 (2012) 187–194.
- [21] L. Dai, S.Z. Zou, *J. Power Sources* 196 (2011) 9369–9372.
- [22] C.X. Xu, Y.Q. Liu, J.P. Wang, H.R. Geng, H.J. Qiu, *J. Power Sources* 199 (2012) 124–131.
- [23] K.H. Park, Y.W. Lee, S.W. Kang, S.W. Han, *Chem. Asian J.* 6 (2011) 1515–1519.
- [24] S. Hu, S. Ha, L. Scudiero, *Electrochim. Acta* 105 (2013) 362–370.
- [25] N.N. Kariuki, X.P. Wang, J.R. Mawdsley, M.S. Ferrandon, S.G. Niyogi, J.T. Vaughey, D.J. Myers, *Chem. Mater.* 22 (2010) 4144–4152.
- [26] R.F. Wang, Z. Zhang, H. Wang, Z.Q. Lei, *Electrochim. Commun.* 11 (2009) 1089–1091.
- [27] A.X. Yin, X.Q. Min, W. Zhu, W.C. Liu, Y.W. Zhang, C.H. Yan, *Chem. Eur. J.* 18 (2012) 777–782.
- [28] T. Cochell, A. Manthiram, *Langmuir* 28 (2012) 1579–1587.
- [29] C.H. Cui, X.J. Liu, H.H. Li, M.R. Gao, H.W. Liang, H.B. Yao, S.H. Yu, *ChemCatChem* 4 (2012) 1560–1563.
- [30] W. Li, X. Zhao, T. Cochell, A. Manthiram, *Appl. Catal. B: Environ.* 129 (2013) 426–436.
- [31] G.Q. Chen, M.Y. Liao, B.Q. Yu, Y.H. Li, D. Wang, G.R. You, C.J. Zhong, B.H. Chen, *Int. J. Hydrogen Energy* 37 (2012) 9959–9966.
- [32] Y. Wang, F.F. Shi, Y.Y. Yang, W.B. Cai, *J. Power Sources* 243 (2013) 369–373.
- [33] T.Y. Jeon, K.S. Lee, S.J. Yoo, Y.H. Cho, S.H. Kang, Y.E. Sung, *Langmuir* 26 (2010) 9123–9129.
- [34] B. Fang, N.K. Chaudhari, M.S. Kim, J.H. Kim, J.S. Yu, *J. Am. Chem. Soc.* 131 (2009) 15330–15338.
- [35] Y.G. Yan, Q.X. Li, S.J. Huo, M. Ma, W.B. Cai, M. Osawa, *J. Phys. Chem. B* 109 (2005) 7900–7906.
- [36] V. Mazumder, S.H. Sun, *J. Am. Chem. Soc.* 131 (2009) 4588–4589.
- [37] T. Cochell, W. Li, A. Manthiram, *J. Phys. Chem. C* 117 (2013) 3865–3873.
- [38] G.J. Zhang, Y.E. Wang, X. Wang, Y. Chen, Y.M. Zhou, Y.W. Tang, L.D. Lu, J.C. Bao, T.H. Lu, *Appl. Catal. B: Environ.* 102 (2011) 614–619.
- [39] A. Cuesta, M. Escudero, B. Lanova, H. Baltruschat, *Langmuir* 25 (2009) 6500–6507.
- [40] A.S. Bauskar, C.A. Rice, *Electrochim. Acta* 93 (2013) 152–157.
- [41] Y.H. Cho, B. Choi, Y.H. Cho, H.S. Park, Y.E. Sung, *Electrochim. Commun.* 9 (2007) 378–381.
- [42] F.J. Vidal-Iglesias, J. Solla-Gullon, E. Herrero, A. Aldaz, J.M. Feliu, *Angew. Chem. Int. Ed.* 49 (2010) 6998–7001.
- [43] M. Wakisaka, S. Mitsui, Y. Hirose, K. Kawashima, H. Uchida, M. Watanabe, *J. Phys. Chem. B* 110 (2006) 23489–23496.
- [44] W.J. Tang, L. Zhang, G. Henkelman, *J. Phys. Chem. Lett.* 2 (2011) 1328–1331.
- [45] L. Xiao, B. Huang, L. Zhuang, J.T. Lu, *RSC Adv.* 1 (2011) 1358–1363.
- [46] J.Y. Wang, Y.Y. Kang, H. Yang, W.B. Cai, *J. Phys. Chem. C* 113 (2009) 8366–8372.
- [47] L.A. Kibler, A.M. El-Aziz, R. Hoyer, D.M. Kolb, *Angew. Chem. Int. Ed.* 44 (2005) 2080–2084.
- [48] B.L. Mojet, S.D. Ebbesen, L. Lefferts, *Chem. Soc. Rev.* 39 (2010) 4643–4655.
- [49] H.A.C.M. Hendrickx, V. Ponec, *Surf. Sci.* 192 (1987) 234–242.
- [50] J.S. Bradley, E.W. Hill, C. Klein, B. Chaudret, A. Duteil, *Chem. Mater.* 5 (1993) 254–256.
- [51] C.H. Cui, H.H. Li, H.P. Cong, S.H. Yu, F.F. Tao, *Chem. Commun.* 48 (2012) 12062–12064.
- [52] S. Koh, P. Strasser, *J. Am. Chem. Soc.* 129 (2007) 12624–12625.
- [53] K. Hartl, M. Hanzlik, M. Arenz, *Energy Environ. Sci.* 4 (2011) 234–238.